Handriani *et al. Nano Convergence* (2026) 13:12
https://doi.org/10.1186/s40580-026-00542-4

Nano Convergence

FULL PAPER

Open Access

Substrate-field-modulated remote-van der Waals hybrid epitaxy in transition metal dichalcogenide heterostructures

Lia Saptini Handriani[1], Suhee Jang[1], Yelim Kim[1], Hyuncheol Yun[1], Dae Yeop Jeong[1], Hyeonsu Park[1], Zhe Gao[1], Jae-il Jang[1] and Won Il Park[1*]

Abstract
Two-dimensional (2D) transition-metal dichalcogenide (TMDC) heterostructures are promising for next-generation optoelectronics, yet the mechanisms controlling their vertical heteroepitaxy remain poorly understood. Here, we systematically investigate metal–organic chemical vapor deposition growth of MoS_2/WS_2 and WS_2/MoS_2 vertical heterostructures across varying interlayer thicknesses (monolayer to multilayer) and substrates (Si, SiO_2 and c-sapphire). We identify a substrate-field-modulated "remote–van der Waals (vdW) hybrid epitaxy" regime, in which vertical overgrowth is confined to a narrow thickness window (~ 1–3 layers), with nucleation density strongly influenced by substrate polarity and defect chemistry. High-resolution STEM reveals that, in the regions where vertical growth occurs, the in-plane crystallographic registry is primarily governed by vdW coupling to the 2D template, yielding a highly preferred single-orientation registry across the examined regions for both stacking orders. This dual-control mechanism decouples growth propensity from epitaxial alignment, providing a scalable framework for synthesizing high-quality 2D vertical heterostructures with precisely engineered interfaces.

Keywords Transition metal dichalcogenides (TMDCs), Vertical heterostructures, Remote epitaxy, Van der Waals epitaxy, Remote–vdW hybrid epitaxy, Two-dimensional materials, MOCVD growth, Nucleation kinetics

1 Introduction

Atomically thin two-dimensional (2D) semiconductor materials, such as transition-metal dichalcogenides (TMDCs), have attracted significant attention owing to their tunable bandgaps, strong light-matter interactions, and compatibility with heterogeneous integration. Despite their reduced dimensionality, these materials support rich electronic and optical phenomena, making them highly promising for applications in optoelectronics, photonics, spin/valleytronics, and quantum technologies [1–9]. Integrating different TMDC layers into 2D heterostructures (HSs) further extends this versatility, enabling interlayer excitons and charge transfer [10–12], enhanced light absorption, and gate-tunable correlated and topological phases that do not exist in the constituent monolayers [13–16].

TMDC HSs are typically classified into vertical HSs, formed by stacking distinct TMDC layers, and lateral HSs, formed by seamless in-plane junctions between different TMDC domains. Mechanical exfoliation offers high-quality single-crystal layers for fundamental studies such as unconventional superconductivity and topological insulator states [17, 18]. However, it remains intrinsically difficult to scale and does not readily provide

---

*Correspondence:
Won Il Park
wipark@hanyang.ac.kr

Full list of author information is available at the end of the article

Graphical abstract

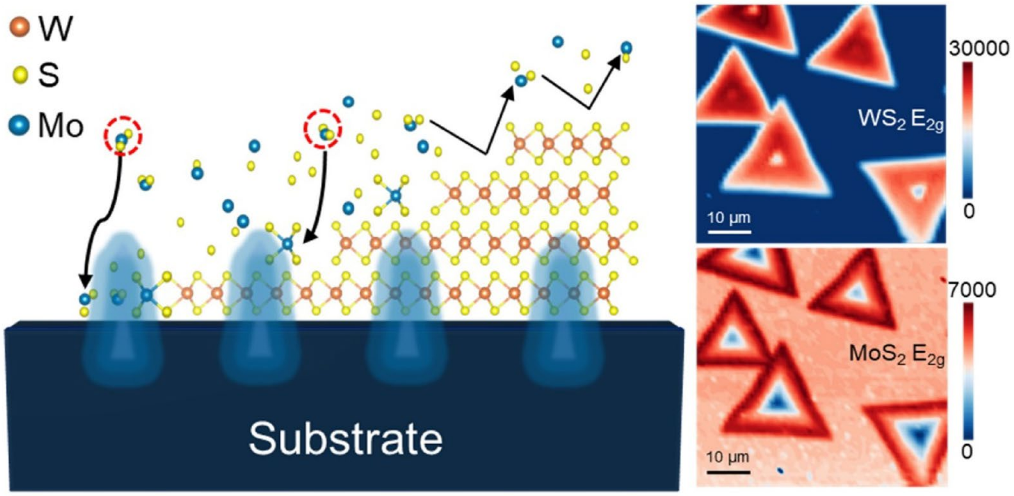

wafer-level control over layer thickness, spatial placement, and crystallographic orientation.

In contrast, chemical vapor deposition (CVD), including metal–organic CVD (MOCVD), has emerged as a scalable route to TMDC HSs with wafer-scale coverage and thickness control [19]. By tuning precursor concentration, temperature, and pressure, CVD growth can be steered towards either lateral or vertical HS formation. Experiments indicate that nucleation, adatom diffusion, and crystallinity are strongly influenced by interfacial defects and surface compatibility [20–27]. Despite these advances, the mechanisms governing vertical 2D-on-2D heteroepitaxy—particularly between atomically smooth, chemically inert basal planes—remain insufficiently understood.

Extensive studies have shown that atomically thin materials only partially screen their substrates and remain effectively "transparent" to the underlying surface. As a result, hydrophilicity, electric double-layer structure, charge doping, and even lattice potential can still be strongly influenced by the underlying support, even through monolayer graphene or other 2D sheets [28–32]. This partial transparency indicates that the presence of a 2D interlayer does not fully decouple a material from its substrate and that substrate-induced fields and chemistry can still be communicated through atomically thin layers. As the intermediate layer becomes thicker, however, the substrate influence is progressively screened. In conventional van der Waals (vdW) epitaxy, the overlayer typically grows on thick, dangling-bond–free vdW surfaces [33, 34]. Such chemically passive surfaces allow the overlayer to be guided mainly by weak vdW interactions, enabling tolerance to substantial lattice mismatch. However, when the interlayer is reduced to an atomically thin 2D sheet on a polar or ionic substrate, the substrate potential can penetrate the spacer and imprint its lattice on the overgrown film, leading to the notion of remote epitaxy [35–39].

To date, vdW and remote epitaxy concepts have been explored predominantly for 3D or quasi-3D heteroepitaxial films grown on 2D layer-coated substrates, where the emphasis is on enabling lattice-mismatched integration and mechanical release. In contrast, how substrate properties and interlayer thickness jointly control nucleation, growth kinetics and crystallographic registry in fully 2D–2D vertical HSs remains much less systematically explored.

In this work, we address these open questions by systematically examining vertical crystal growth in a fully 2D–2D system using MOCVD. We grow MoS_2/WS_2 and WS_2/MoS_2 vertical heterostructures on Si, SiO_2 and c-sapphire, examining overgrowth across various 2D interlayer thicknesses (from monolayer to multilayer). From these observations, we identify a dual-control regime, which we term substrate-field-modulated remote–van der Waals hybrid epitaxy (remote–vdW hybrid epitaxy). In this regime, the substrate's electrostatic field and defect chemistry govern the nucleation density and the active thickness window (1–3 layers) for overgrowth, whereas the in-plane crystallographic registry is dictated primarily by the 2D template through van der Waals coupling. This hybrid mechanism—bridging remote and van der Waals epitaxy—enables the synthesis of single-orientation 2D vertical heterostructures with a highly preferred single-orientation registry and no detectable mirror-twin signatures within the representative sampled areas. This provides a practical, scalable framework for the large-area growth of high-quality TMDC heterostructures with engineered interfaces.

2 Methods

2.1 Synthesis of MoS_2/WS_2 vertical heterostructures

2.1.1 Growth of WS_2 templates on SiO_2/Si

Triangular WS_2 flakes were synthesized on SiO_2/Si substrates using a custom-built vertical cold-wall MOCVD reactor equipped with a rotating graphite susceptor. Tungsten hexacarbonyl ($W(CO)_6$, WHC) and diethyl sulfide ($(C_2H_5)_2S$, DES) served as tungsten and sulfur precursors, respectively. The solid WHC and liquid DES were maintained in temperature-controlled bubblers at 30 °C and 55 °C and delivered into the quartz-tube reactor using Ar carrier gas [25, 26].

To promote large-domain growth, a NaCl-assisted strategy was employed by placing a circular crucible containing 0.6 g of NaCl (Sigma-Aldrich) at the center of the susceptor. Growth was conducted at 650 °C and 5 Torr for 20 min, with WHC and DES introduced at equal flow rates (6 sccm each) under a background flow of 140 sccm Ar and 10 sccm H_2. The as-grown WS_2 flakes were subsequently used as templates for MoS_2 overgrowth in the MoS_2/WS_2 configuration.

2.2 *MoS_2 overgrowth on WS_2/SiO_2*

MoS_2/WS_2 vertical heterostructures were obtained by a second MOCVD step in the same reactor. Molybdenum hexacarbonyl ($Mo(CO)_6$) and DES were used as Mo and S precursors, respectively. $Mo(CO)_6$ was held at 30 °C in a temperature-controlled bubbler and delivered by Ar carrier gas, while DES was supplied from a liquid bubbler. The reactor temperature, pressure and carrier-gas flows were kept identical to those used for WS_2 template growth (650 °C, 5 Torr, 140 sccm Ar, 10 sccm H_2). Crucially, no NaCl or other transport agents were introduced during this second step to ensure that the MoS_2 overgrowth was governed solely by the template-substrate interaction.

The $Mo(CO)_6$ and DES flow rates were adjusted to maintain a sulfur-rich environment, and growth times in the range of 30–60 min were used to form MoS_2 overlayers on the WS_2/SiO_2 templates. These samples, which contain WS_2 thickness gradients ($n = 0$ to multilayer), were used for the thickness- and time-dependent MoS_2 overgrowth studies presented in Sect. 3.1 of the main text.

2.3 Synthesis of WS_2/MoS_2 vertical heterostructures

2.3.1 Preparation of thickness-graded MoS_2 templates by Au-assisted exfoliation

For the reciprocal WS_2/MoS_2 configuration, thickness-graded MoS_2 templates were prepared by gold-assisted mechanical exfoliation. A metal adhesion stack of Ti/Au (2 nm/15 nm) was deposited onto p-type Si substrates with a 300 nm SiO_2 layer using an electron-beam evaporator (Woosin CryoVac) at a deposition rate of 0.5 $Å\cdot s^{-1}$. Commercial bulk MoS_2 crystals (HQ Graphene; 2D Semiconductors) were exfoliated using adhesive tape and brought into conformal contact with the Au-coated substrates.

To enhance the yield of large-area monolayers, the substrate was heated to 130–150 °C for ~ 90 s during contact, followed by a ~ 60 s cooling period before tape removal. The underlying Ti/Au layer was then removed using an aqueous KI/I_2 etchant, and the samples were annealed at 350 °C for 2 h in H_2 atmosphere to remove organic residues and improve interface cleanliness. This procedure produced MoS_2 flakes spanning monolayer to multilayer thicknesses (n = 1–multilayer), which served as templates for reciprocal WS_2 overgrowth on SiO_2/Si and for substrate-comparison experiments on Si and c-sapphire.

2.4 *WS_2 overgrowth on exfoliated MoS_2 templates*

WS_2/MoS_2 vertical heterostructures were grown in the same vertical MOCVD reactor used for WS_2 template synthesis. WHC and DES were supplied from temperature-controlled bubblers (30 °C for WHC, 55 °C for DES) and introduced at equal flow rates of 6 sccm under 140 sccm Ar and 10 sccm H_2 at 650 °C and 5 Torr. WS_2 was deposited on the Au-assisted exfoliated MoS_2 templates described above, which span monolayer to multilayer thicknesses.

Growth times in the range of 7–15 min were used to capture the early nucleation and vertical build-up of WS_2 on MoS_2, while longer growths were employed for the fully developed WS_2/MoS_2 stacks analyzed in the main text. For substrate-comparison experiments, identically prepared MoS_2 templates were transferred onto Si, SiO_2 and c-sapphire and subjected to the same WS_2 growth conditions, allowing direct assessment of substrate-field effects at fixed MoS_2 thickness.

2.5 Optical and structural characterization

The morphology and layer contrast of MOCVD-grown WS_2 templates, MoS_2/WS_2 heterostructures and WS_2/MoS_2 stacks were first examined by optical microscopy (Olympus BX51). Atomic force microscopy (AFM) was used to determine step heights and verify the layer number of exfoliated MoS_2 and MOCVD-grown WS_2 flakes, as well as to compare the apparent MoS_2 thickness on WS_2 versus SiO_2 (Figs. S3 and S4).

Room-temperature Raman and photoluminescence (PL) measurements were performed using a micro-Raman system (Dongwoo Optron) equipped with a 532 nm excitation laser and 50 × /100 × objective lenses. Raman and PL mapping was carried out on predefined grids to resolve thickness-dependent growth windows and excitonic behavior. Spectral datasets were processed using baseline subtraction followed by multi-Gaussian peak fitting, as described in Supplementary Note 1, to deconvolute overlapping MoS_2 and WS_2 modes and obtain reliable intensity and peak-position maps.

For structural analysis at the nanoscale, high-resolution transmission electron microscopy (HR-TEM, JEOL JEM-F200, 200 kV) was used to assess lattice crystallinity and acquire selected-area electron diffraction (SAED) patterns over micrometer-scale regions. Atomic-scale interface structure, stacking registry and local moiré superlattices were examined by spherical-aberration-corrected high-angle annular dark-field scanning TEM (HAADF-STEM, JEOL JEM-ARM200F, 80 kV). Cross-sectional lamellae were prepared using a focused ion beam (FIB, FEI Helios 650) to directly visualize the vertical heterostructure geometry, confirm the presence or absence of WS_2 overgrowth on MoS_2 templates of different thicknesses, and perform elemental mapping via energy-dispersive X-ray spectroscopy (EDS).

3 Results and discussion

3.1 Thickness-selective and time-dependent MoS_2 overgrowth on WS_2/SiO_2

Triangular WS_2 flakes were synthesized on SiO_2/Si substrates in our vertical MOCVD reactor using NaCl as a growth promoter (Methods). The addition of NaCl facilitates the formation of volatile tungsten oxychlorides, which enhances precursor mass transport and reduces nucleation density [40]. This strategy significantly increased both the lateral size and the crystalline quality of the WS_2 flakes, providing large, continuous domains necessary for spatially resolved heterostructure studies. These WS_2 flakes were subsequently used as interlayers to investigate the growth behavior of MoS_2, as illustrated in Fig. 1a. OM images (Fig. 1b) reveal triangular domains up to ~ 35 μm across with clear thickness contrast, providing a platform to examine overgrowth as a function of WS_2 layer number n.

To quantify MoS_2 overgrowth across a thickness-gradient flake, we processed the Raman mapping dataset (2,601 spectra across a 51 × 51 grid) using baseline subtraction followed by multi-Gaussian fitting (Supplementary Note 1). This approach enables robust deconvolution of overlapping features, particularly resolving the MoS_2 A_{1g} (~ 401 cm^{-1}) mode adjacent to the WS_2 A_{1g} (~ 414 cm^{-1}) peak under a spatially varying background. By more realistically separating the contributions of individual peaks, this multi-Gaussian analysis improves the reliability of both the Raman spectra and the resulting intensity maps.

After 60 min of MoS_2 deposition, representative fitted spectra extracted from the marked locations in Fig. 1b are shown in Fig. 1c. The WS_2 layer number n was assigned from the A_{1g}–E_{2g} separation (Δω), which increases from ~ 66 cm^{-1} for monolayer WS_2 ($n = 1$) to ~ 73 cm^{-1} for multilayer WS_2 ($n \geq 4$), consistent with prior reports [41]. On this WS_2 thickness-graded template, MoS_2 peaks are observed on bare SiO_2 ($n = 0$) and on thin WS_2 ($n = 1$–3). In contrast, multilayer WS_2 ($n \geq 4$) shows only WS_2 modes, with no detectable MoS_2 signal (Fig. 1c). The corresponding Raman intensity maps (Fig. 1d,e) visualize this thickness-dependent growth window; the WS_2 E_{2g} map delineates the WS_2 template, whereas the MoS_2 E_{2g} map shows overgrowth confined to bare SiO_2 and thin WS_2, with negligible signal on multilayer regions.

PL provides a complementary probe of this thickness-dependent behavior. The spectra in Fig. 1f show that the excitonic emission near ~ 2.0 eV is strongest when MoS_2 is deposited on monolayer WS_2 ($n = 1$) and decreases for $n = 2$–3, whereas it is weaker on bare SiO_2 ($n = 0$) and becomes minimal on multilayer WS_2 ($n \geq 4$). Consistently, the PL map integrated at ~ 2.0 eV (Fig. 1g) reproduces the same thickness-dependent intensity variation across the flake, while the peak-position map (Fig. 1h) remains comparatively uniform. These results indicate that MoS_2 grown on thin WS_2 experiences reduced non-radiative quenching and improved optical quality compared with MoS_2 on bare SiO_2 [42–44]. In line with this picture, atomic force microscopy (AFM) measurements (Supplementary Note 2) show that the apparent MoS_2 thickness increases more rapidly on SiO_2 than on bilayer WS_2, consistent with slower vertical build-up on the chemically inert WS_2 surface, as schematically summarized in Fig. S3c.

To understand whether this thickness dependence is governed by growth kinetics, we performed time-resolved Raman measurements during MoS_2 deposition on WS_2/SiO_2 (Fig. 2). Raman maps acquired after 30 and 60 min capture how the overgrowth evolves across regions of different WS_2 thickness (Fig. 2b,c). As the growth time increases, the MoS_2 E_{2g} and A_{1g} signals increase on bare SiO_2 ($n = 0$) and on monolayer WS_2 ($n = 1$), whereas the spectra collected on multilayer WS_2 ($n \geq 4$) retain only the WS_2 modes with no appreciable MoS_2 contribution. Statistics extracted from the maps (Fig. 2d,e) quantify this trend, showing continued growth of MoS_2 on $n = 0$ and $n = 1$, but persistently negligible MoS_2 intensity on multilayer WS_2. We interpret this increase in Raman intensity as a progressive accumulation of MoS_2, representing a composite process of lateral coverage expansion and subsequent vertical stacking. To differentiate between these factors, we corroborated the Raman trends with AFM topographic analysis (Supplementary Note 2), which independently verifies that the rising spectroscopic signal accompanies an actual increase in physical film height. These data indicate that, within the growth times probed here,

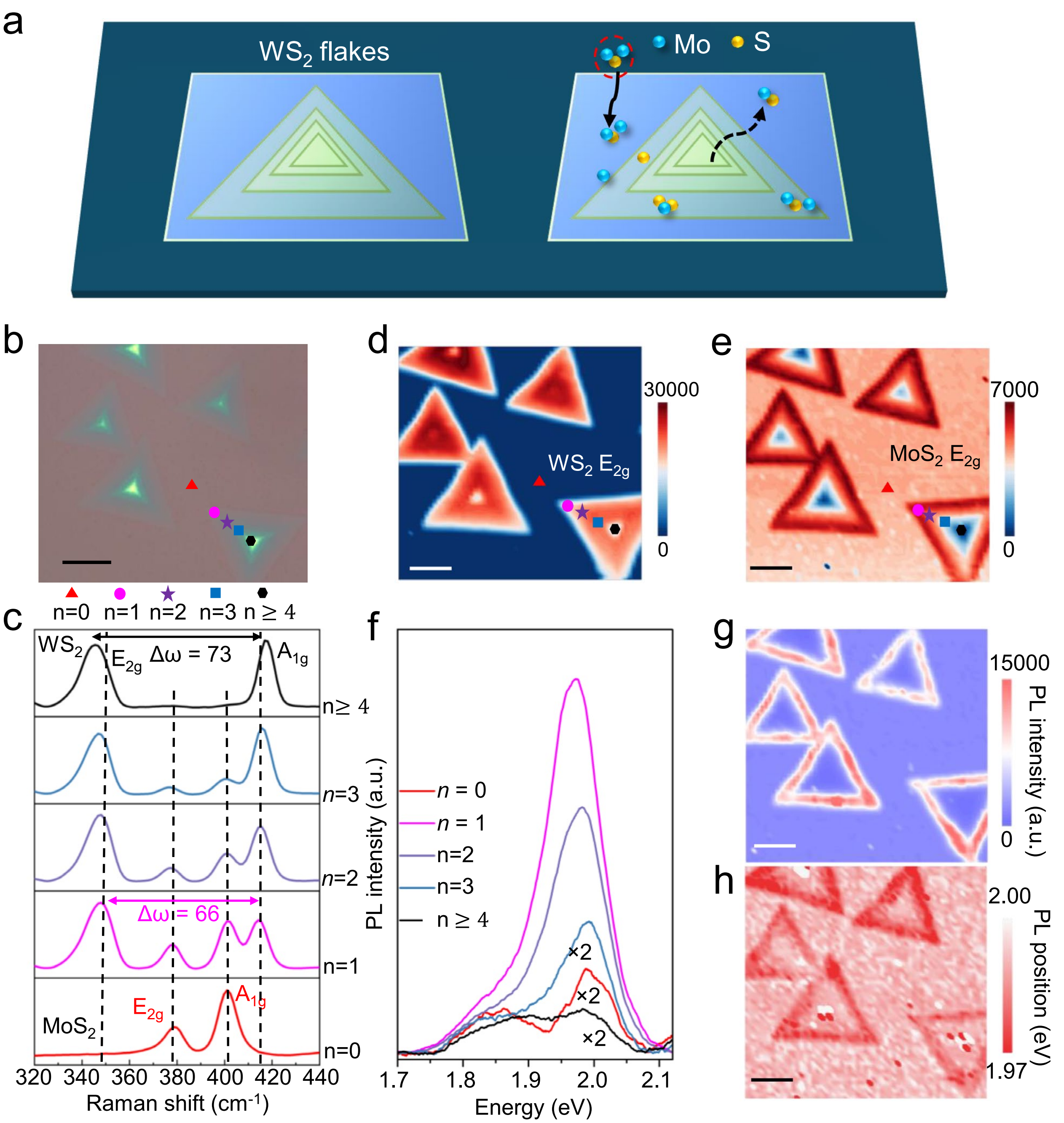

Fig. 1 Thickness-dependent heterostructure growth of MoS_2 on WS_2 templates. **a**, Schematic illustration of the vertical MOCVD growth of MoS_2 on a triangular WS_2 flake supported on SiO_2/Si. **b**, Optical microscopy image of a representative WS_2 flake showing contrast variations corresponding to different layer thicknesses (*n*). **c**, Representative Raman spectra extracted from the marked spots in (b), showing distinct MoS_2 signatures on bare SiO_2 ($n = 0$) and thin WS_2 ($n = 1$–3), but absent signals on multilayer WS_2 ($n \geq 4$). **d**, **e**, Raman intensity maps of the WS_2 E_{2g} (template) and MoS_2 E_{2g} (overlayer) modes, respectively, visualizing the confinement of vertical growth to the atomically thin regions. **f**–**h**, Corresponding PL spectra (f), integrated intensity map (g), and peak position map (h) of the A exciton, confirming strong MoS_2 emission from the monolayer/bilayer regions and suppression on the multilayer center**.** Scale bars in b, d–e, and g–h: 10 μm

material accumulation continues only on bare SiO_2 and atomically thin WS_2, while multilayer templates remain effectively inactive for MoS_2 growth. This thickness-selective evolution suggests that the buried substrate can still influence the effective growth environment through an atomically thin WS_2 interlayer, but this influence becomes strongly attenuated once the WS_2 exceeds a few layers in thickness.

To quantify the physical length scale of this thickness-dependent selectivity, we evaluated the Debye screening

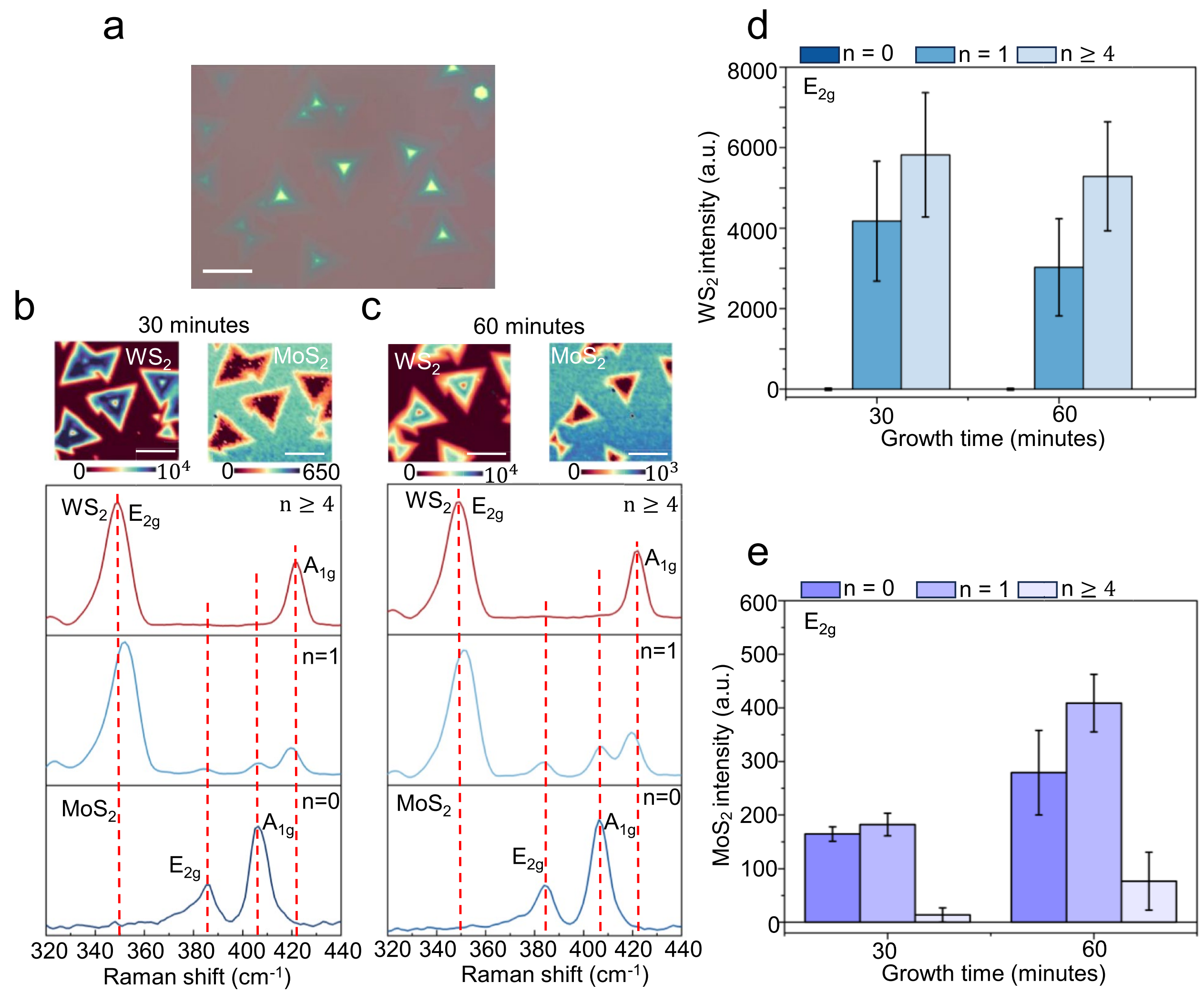

Fig. 2 Time-resolved evolution of MoS_2 vertical growth kinetics on WS_2/SiO_2. **a**–**c**, Raman intensity maps of the MoS_2 E_{2g} mode acquired after different growth durations (30 min and 60 min), visualizing the progressive accumulation of MoS_2 material. The maps reveal that overgrowth proceeds continuously on bare SiO_2 ($n=0$) and monolayer WS_2 ($n=1$) regions, whereas multilayer WS_2 regions ($n \geq 4$) show negligible MoS_2 signal regardless of growth time. **d**, **e**, Statistical distributions of MoS_2 Raman peak intensities extracted from the mapping data, quantifying the continued vertical growth on atomically thin templates versus the persistent suppression on thick WS_2 layers over the 60-min period. Scale bars: 20 μm. Note that intensity values in non-growth regions were clamped to zero to remove baseline subtraction noise

length λ_D of the TMDC template at the growth temperature (650 °C). By considering the thermal activation of carriers and the specific out-of-plane dielectric constant of the TMDC lattice [45], the estimated λ_D ranges from 0.7 to 2.2 nm. This theoretical range matches the observed active window of ~ 1–3 layers (~ 0.65–1.95 nm), supporting the interpretation that vertical nucleation is governed by the penetration of the substrate's electrostatic field, which becomes effectively screened as the interlayer thickness exceeds a few Debye lengths (see Supplementary Note 3 for detailed calculations). Our observation of field penetration through monolayer WS_2 is consistent with previous reports on the 'dielectric transparency' of 2D materials. Theoretical and experimental studies have shown that the screening capability of monolayer TMDCs is significantly reduced compared to their bulk counterparts due to the dimensional confinement of electric field lines [46, 47]. Consequently, the underlying substrate can exert a strong, uniform electrostatic influence through the monolayer—an effect that is fundamentally distinct from localized defect-mediated interactions.

3.2 Substrate-dependent nucleation on atomically thin WS_2 interlayers

To isolate the role of the underlying substrate at fixed interlayer thickness, we compared MoS_2 overgrowth on monolayer WS_2 ($n=1$) supported on Si, SiO_2 and c-sapphire (Fig. 3a–c). For the same WS_2 interlayer, the MoS_2 A_{1g} intensity—a proxy for growth yield—is highest on

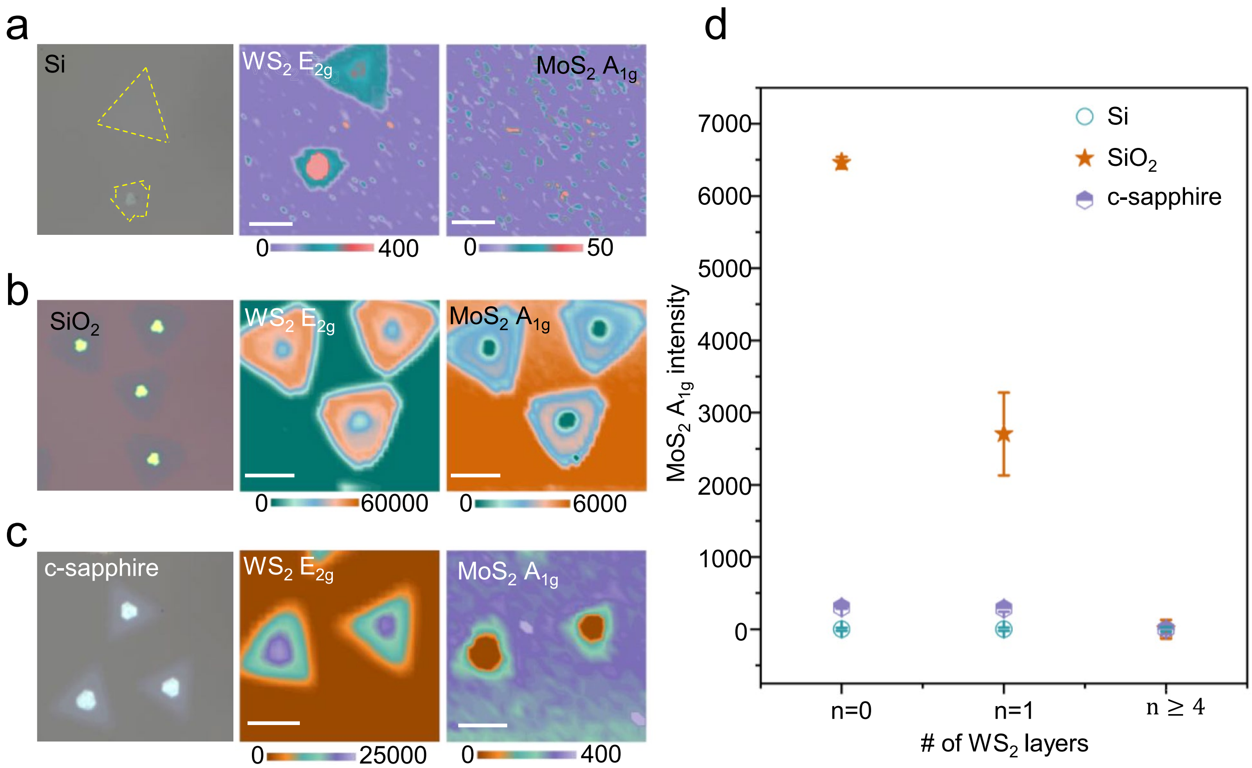

Fig. 3 Substrate-dependent nucleation hierarchy of MoS_2 on atomically thin WS_2 interlayers. **a**–**c**, Representative Raman spectra and optical images comparing MoS_2 overgrowth on monolayer WS_2 ($n = 1$) supported by three different substrates: Si, SiO_2 and c-sapphire. The data reveal a distinct growth hierarchy where nucleation is most abundant on SiO_2, intermediate on sapphire, and negligible on Si. **d**, Statistical summary of MoS_2 growth yield versus WS_2 interlayer thickness (n). The trends confirm that the substrate influence is transmitted through thin interlayers ($n = 1$–3) to modulate growth, but is fully screened by thicker multilayers ($n \geq 4$), leading to suppressed growth regardless of the substrate. Scale bars: 10 µm

WS_2/SiO_2, intermediate on WS_2/c-sapphire, and nearly negligible on WS_2/Si. When this comparison is extended across the WS_2 thickness series, all three systems show suppression of MoS_2 on multilayer WS_2 ($n \geq 4$). However, in the atomically thin limit ($n = 0$–1), the growth yield remains strongly substrate dependent and is nearly suppressed on Si (Fig. 3d).

The observed growth hierarchy, $WS_2/SiO_2 > WS_2$/c-sapphire $\gg WS_2$/Si, is fundamentally rooted in the intrinsic electrostatic landscape and surface potential of the underlying substrates. Amorphous SiO_2 presents a polar oxide surface characterized by a high density of silanol (Si–OH) groups and occasional under-coordinated defects. For bare SiO_2 ($n = 0$), these surface hydroxyls act as potent chemical anchors: they facilitate the chemisorption of metal–organic precursors through specific surface reactions (e.g., proton transfer or ligand exchange), effectively locking the adatoms in place via strong covalent Mo–O–Si bonds [48–50]. This site-specific chemical trapping significantly lowers the nucleation energy barrier but simultaneously restricts adatom diffusion, leading to the rapid, random "self-seeding" of polycrystalline domains observed on the oxide [51].

In marked contrast, the ionic c-sapphire surface lacks these random chemical traps. Instead, it presents a periodic electrostatic potential that facilitates longer adatom diffusion lengths across a relatively smooth energy landscape. This interpretation is supported by molecular dynamics simulations [52], which demonstrate that crystalline substrates like sapphire exhibit lower energy barriers for adatom migration compared to amorphous oxides. This promotes migration to energetically favorable sites rather than dense stochastic nucleation, resulting in an intermediate growth yield.

Finally, the crystalline Si surface exhibits negligible growth, a behavior attributed to its non-polar, covalent nature. Unlike ionic or hydroxylated surfaces, the neutral Si lattice lacks strong electrostatic dipoles or polar moieties required to anchor the initial precursor molecules [48]. Consequently, the surface exhibits a low adsorption energy, causing reactant molecules to desorb before they can nucleate. We note that Si is typically covered by a thin native oxide; however, its much lower density of hydroxyl terminations and weaker interfacial dipoles compared to thermally grown SiO_2 provide insufficient chemical/electrostatic anchoring to stabilize nuclei under our high-temperature MOCVD conditions. This confirms that the substrate's active (polar/chemical) versus passive (non-polar/inert) character largely dictates the nucleation probability.

Crucially, the preservation of this hierarchy even beneath a WS_2 interlayer indicates that substrate-specific potentials are not neutralized but are instead transmitted through the atomically thin 2D sheet. For the WS_2-covered substrates ($n = 1$), direct chemical bonding to the underlying substrate is blocked by the inert vdW surface of WS_2; instead, the mechanism involves remote electrostatic modulation. Here, substrate-dependent fields (e.g., from polar hydroxyls and defects on SiO_2) partially penetrate the thin interlayer and locally increase the adsorption energy of precursors on the TMDC surface. These results suggest that an atomically thin WS_2 layer acts as an electrostatic window, allowing substrate-polarity and defect-related fields to 'leak' through and locally modulate the growth landscape on the chemically inert TMDC surface. As the interlayer becomes thicker than a few layers ($n \geq 4$), this substrate influence is largely suppressed by the cumulative screening of the TMDC layers, consistent with the thickness-selective overgrowth behavior described in Sect. 3.1.

As discussed below (Sect. 3.3), atomic-resolution STEM further confirms that the TMDC template remains structurally coherent and continuous in growth-active regions, supporting a mechanism dominated by remote modulation of adsorption/chemisorption barriers rather than template defect creation. This substrate-mediated coupling is reminiscent of remote epitaxy, in which the electrostatic potential of a polar or ionic substrate penetrates an ultrathin 2D spacer and can still affect the growth of the overgrown film [36].

3.3 Atomic-scale registry and remote–vdW hybrid epitaxy in MoS_2/WS_2

Having established that the substrate influences where MoS_2 can grow through an atomically thin WS_2 interlayer (Sects. 3.1 and 3.2), we next examine how the WS_2 itself controls the in-plane crystallographic alignment of the overgrown MoS_2. To provide a comprehensive assessment, we first performed a large-area HAADF-STEM survey of a triangular MoS_2 overgrown across a thickness-modulated WS_2 template, spanning monolayer ($n = 1$) to multilayer ($n \geq 4$) regions (Fig. 4a). The preservation of a single crystallographic orientation across these thickness steps is initially confirmed by reciprocal-space analysis; SAED patterns acquired from the $n = 1$, $n = 2$, and interfacial regions all exhibit a single set of sharp hexagonal $(10\,\bar{1}\,0)$ reflections with no detectable spot splitting or rotation (Fig. 4c).

To probe the atomic-scale registry, we examined a representative region where MoS_2 grows across the 1L–2L WS_2 boundary (red box in Fig. 4a). Atomically resolved HAADF-STEM images (Fig. 4d, e) show that the in-plane lattice orientation is preserved across the thickness transition, with no contrast reversal or phase shift characteristic of a 60° mirror-twin boundary. The atomic lattice remains continuous across the boundary, with a comparable in-plane spacing (~ 0.28 nm) on both sides, indicating that MoS_2 maintains a single in-plane registry (i.e., a single-domain registry) across the 1L–2L WS_2 transition.

Crucially, the registry between the layers is quantitatively verified by atomic intensity line profiles extracted from the $n = 1$ and $n = 2$ regions (Fig. 4f). The profiles for MoS_2 on 1L WS_2 (magenta) and 2L WS_2 (green), resolve the distinct Mo, W, and S columns with high precision. The atomic-column assignment (Mo/W/S) and the stacking-order interpretation for Fig. 4f were validated by multislice HAADF-STEM simulations (Dr. Probe) under matching imaging conditions (Supplementary Note 6; Figs. S11–S12). The periodic intensity peaks confirm that the Mo atomic columns of the overlayer precisely follow the periodic arrangement of the underlying tungsten (W) atoms of the template in both regions.

Collectively, these real- and reciprocal-space observations demonstrate that MoS_2 forms a single-orientation film that remains crystallographically aligned to the WS_2 template over the thickness step, consistent with a vdW epitaxial relationship between the two TMDC layers. Notably, these atomic-resolution STEM observations also show that the WS_2 template remains structurally coherent and continuous in the growth-active regions, with no indication of template degradation that would be expected for defect-mediated nucleation pathways. This supports an interpretation in which the substrate primarily biases the adsorption/chemisorption energy landscape (and thus the sticking coefficient and residence time of adatoms) on a structurally intact 2D surface, rather than generating new template defects as nucleation centers.

Building on this vdW epitaxial alignment and on the thickness- and substrate-dependent growth behavior in Figs. 1–3, we describe our system within a substrate-mediated remote–vdW hybrid picture (Fig. 4g). In classic remote epitaxy, the overlayer can inherit lattice registry directly from the buried substrate because the substrate's electrostatic potential penetrates an ultrathin 2D spacer [35, 36]. In our fully 2D–2D stacks, by contrast, the in-plane orientation is set by vdW epitaxy to the crystalline WS_2 interlayer, while substrate-mediated fields primarily modulate adatom adsorption and the subsequent probability and density of nucleation—thereby determining where vertical growth is enabled (for thin interlayer) or suppressed (for thick interlayer). In this sense, our observations extend remote-epitaxy concepts to a "remote–vdW hybrid" regime in which the 2D interlayer fixes the epitaxial registry, whereas the buried substrate tunes the local growth propensity.

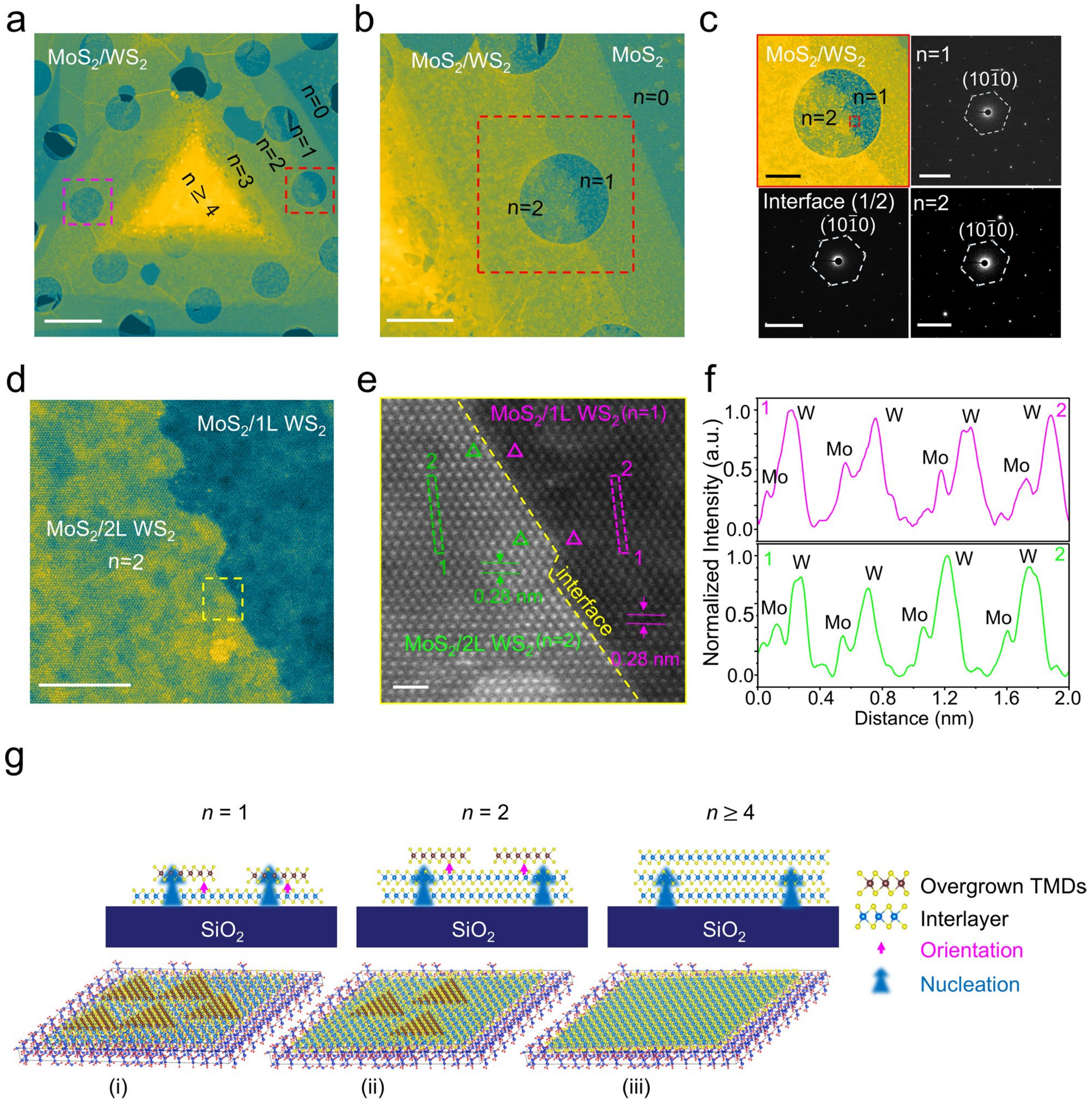

Fig. 4 Verification of vdW-dictated registry and the hybrid growth model. **a**, HAADF-STEM survey of a large-area triangular MoS_2 flake overgrown across a thickness-modulated WS_2 template, spanning from monolayer ($n=1$) to multilayer ($n \geq 4$) regions (scale bar: 2 µm). **b**, Magnified HAADF-STEM view of the interface region (scale bar: 1 µm). **c**, SAED patterns acquired from the $n=1$, $n=2$, and interfacial regions, confirming a single set of sharp ($10\bar{1}0$) hexagonal reflections and invariant crystallographic orientation across thickness boundaries (scale bars: 500 nm; diffraction spot scale: 5 nm.$^{-1}$). **d**, Magnified HAADF-STEM view of the interface region (corresponding to the red dashed box in **c**) showing the boundary between MoS_2/1L WS_2 ($n=1$) and MoS_2/2L WS_2 ($n=2$) regions (scale bar: 10 nm). **e**, Atomic-resolution HAADF-STEM image of the interfacial area (corresponding to the yellow dashed box in **d**), revealing the atomically sharp boundary between MoS_2/1L WS_2 and MoS_2/2L WS_2 with preserved lattice registry (scale bar: 2 nm). **f**, Atomic intensity line profiles corresponding to the dash lines in **e**. The profiles for MoS_2 on 1L WS_2 (magenta) and 2L WS_2 (green) show continuous, periodic atomic-column contrast across the boundary, consistent with an intact stacked heterostructure. **g**, Schematic of the remote–vdW hybrid epitaxy model, illustrating how the 2D template determines the crystallographic orientation of the overgrown layer while the underlying substrate field modulates the nucleation density across varying template thicknesses ($n=1, 2, \geq 4$)

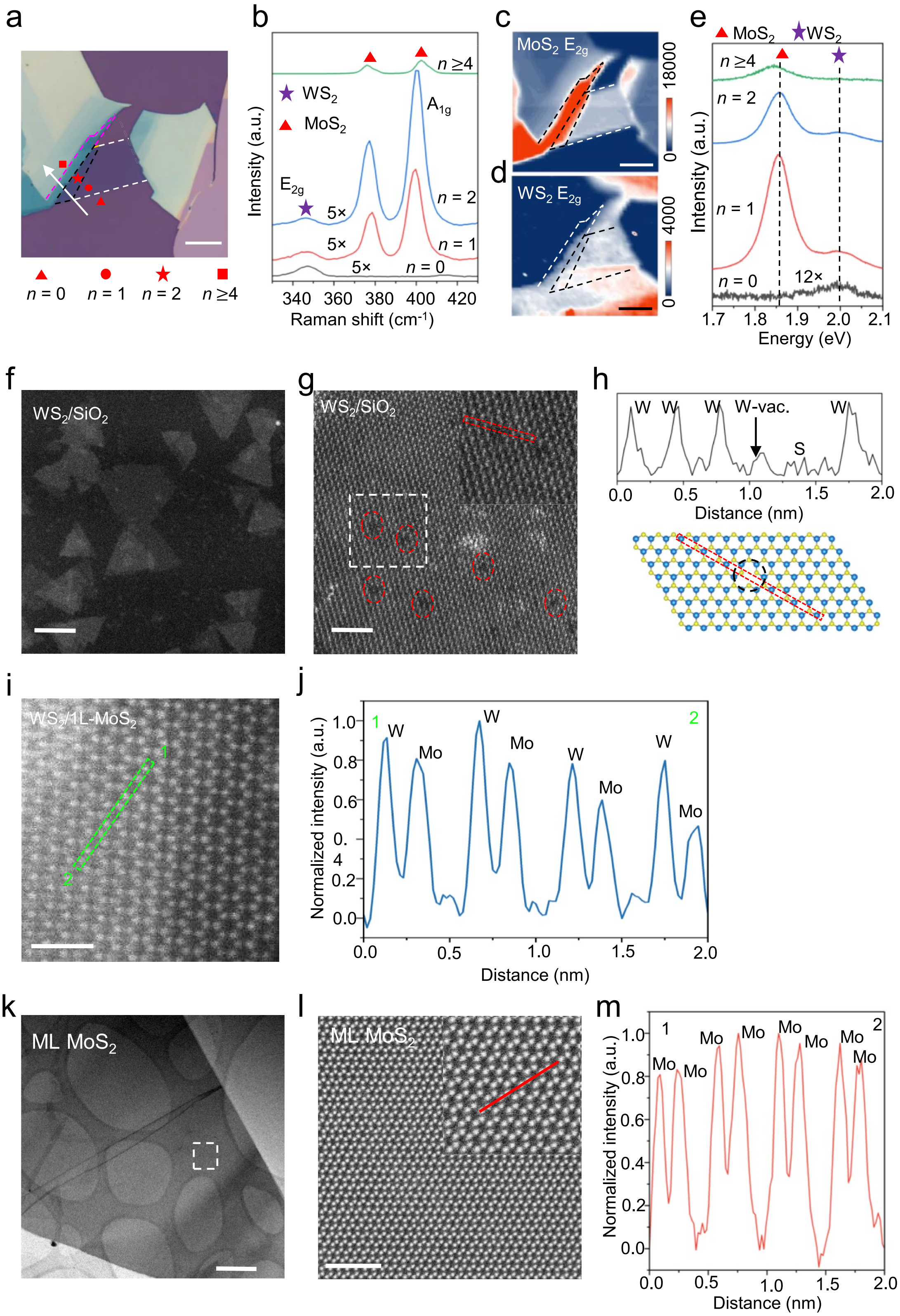

Fig. 5 (See legend on next page.)

(See figure on previous page.)

Fig. 5 Reciprocal growth behavior and atomic-scale microstructure of WS_2/MoS_2 heterostructures. **a**, Optical micrograph of a thickness-graded MoS_2 template used for reciprocal growth. **b**, Raman spectra showing WS_2 nucleation on bare SiO_2 ($n = 0$) and thin MoS_2 ($n = 1$–2), with complete suppression on multilayer MoS_2 ($n \geq 4$). **c**, **d**, Raman intensity maps of the MoS_2 E_{2g} and WS_2 E_{2g} modes, confirming the thickness-selective growth window. **e**, Photoluminescence (PL) spectra showing significant emission enhancement for WS_2 on monolayer ($n = 1$) and bilayer ($n = 2$) MoS_2 compared to SiO_2, and the complete suppression of emission on thick MoS_2 ($n = \geq 4$). **f**–**h**, Atomic-resolution STEM images of WS_2 grown on amorphous SiO_2, revealing polycrystalline triangular islands with abundant point defects. **i**, **j**, Atomic-resolution STEM of WS_2 grown on monolayer MoS_2, showing a continuous lattice with uniform contrast and single in-plane orientation, indicative of coherent heteroepitaxy. **k**–**m**, Atomic-resolution STEM of the multilayer MoS_2 region resolving only the MoS_2 lattice, verifying the effective shut-off of WS_2 nucleation on thick templates. Scale bars: 10 µm (a, c, d); 500 nm (k); 50 nm (f); 2 nm (g, l); 1 nm (i)

Figure 4g schematically summarizes this remote–vdW hybrid picture. Atomically thin WS_2 interlayers allow substrate fields to bias adatom adsorption and nucleation, enabling vertical overgrowth for $n \approx 1$–2 (Fig. 4g (i,ii)). In contrast, thicker WS_2 flakes effectively screen the substrate, so nucleation is strongly suppressed and overgrowth is shut off (Fig. 4g (iii)), consistent with the thickness- and substrate-dependent trends in Figs. 1–3.

3.4 Reciprocal WS_2/MoS_2 growth: generality of remote–vdW hybrid epitaxy

To test whether the remote–vdW hybrid mechanism is specific to MoS_2/WS_2 or extends to the reciprocal stacking order, we inverted the configuration and investigated WS_2 growth on MoS_2 templates (Fig. 5a). Au-assisted exfoliated MoS_2 flakes on SiO_2/Si span thicknesses from monolayer ($n = 1$) to multilayer ($n \geq 4$). Prior to growth, we confirmed these layer assignments by AFM, which yielded a step height of ~ 0.9 nm for the monolayer regions (Supplementary Note 4.1). This precise thickness calibration was then used to label the local layer number n in the optical and Raman maps, allowing us to directly test whether the same thickness-dependent overgrowth window appears in the inverted system.

Consistent with the MoS_2/WS_2 case, WS_2 growth occurs preferentially on bare SiO_2 and atomically thin MoS_2 ($n = 1$–2) and is strongly suppressed on thicker flakes (Fig. 5b–d). Detailed kinetic analysis and substrate-variant experiments (Si, SiO_2, c-sapphire) confirm that this selective, thin layer-confined growth is robust to stacking order and primarily driven by the underlying substrate field (Supplementary Notes 4.2–4.3). This thickness-dependent behavior is further corroborated by PL spectra at corresponding regions (Fig. 5e). The WS_2 emission intensity is significantly higher when grown on monolayer and bilayer MoS_2 templates compared to that grown on the bare SiO_2 substrate, while no WS_2 PL is detected on multilayer MoS_2 ($n \geq 4$). This enhancement on thin templates, consistent with our observations in Sect. 3.1, indicates superior crystalline quality and reduced non-radiative recombination in TMDC films supported by vdW interlayers.

Plan-view TEM and SAED provide complementary, larger-area evidence for this trend, showing well-aligned heteroepitaxial WS_2 on thin MoS_2, in contrast to polycrystalline WS_2 domains on SiO_2 (Supplementary Note 5.1). Within the active thickness window, the MoS_2 template again dictates the microstructure of the overgrown WS_2. On amorphous SiO_2, WS_2 forms polycrystalline triangular islands characterized by a high density of atomic defects. Atomic-resolution STEM images (Fig. 5f–h) reveal numerous point defects, identified as Tungsten vacancies (highlighted by red circles). The corresponding line intensity profile (Fig. 5h, inset) explicitly shows a sharp drop in atomic column intensity at these sites based on Z-contrast, confirming the absence of W atoms. Additionally, the film can locally develop multilayer patches (2L/3L/ML) during growth (Supplementary Note 5.2).

Atomic-resolution images from these regions exhibit pronounced moiré contrast within the thicker patches (Fig. S9c,e), and the corresponding FFT contains two hexagonal spot sets rotated by ~ 20°, indicating twisted WS_2 homo-stacking rather than a single, registry-matched multilayer (Fig. S9g, left panel). The extracted moiré periodicity in the filtered image (Fig. S9g, right panel) is consistent with this twist-derived superlattice, highlighting the rotationally unconstrained stacking that is typical when WS_2 nucleates and thickens on an amorphous oxide surface. The high density of grain boundaries and surface-induced disorder in these polycrystalline domains likely serve as potent non-radiative quenching centers, explaining the weak PL emission observed on SiO_2.

In marked contrast, WS_2 grown on monolayer MoS_2 forms a continuous lattice with highly uniform Mo/W/S column contrast. Line intensity profiles across these regions show consistent atomic intensities with no evidence of the vacancy-induced dips observed on SiO_2 (Fig. 5i,j; Fig. S13). Furthermore, the corresponding FFT confirms a single in-plane orientation indicative of coherent heteroepitaxy. This distinct difference demonstrates that the monolayer template not only aligns the crystal orientation but also strongly suppresses vacancy formation compared to growth on amorphous substrates. This transition from polycrystalline growth on SiO_2 to single-orientation vdW epitaxy on the MoS_2 template effectively minimizes non-radiative decay channels. By providing an atomically smooth, dangling-bond-free surface that screens the overlayer from the underlying substrate's disordered electrostatic landscape, the thin MoS_2 template facilitates the growth of TMDC layers with markedly improved optical quality.

In regions where the underlying MoS_2 exceeds several layers, only the MoS_2 lattice is resolved, with no additional periodic contrast attributable to WS_2 (Fig. 5j–l), confirming that WS_2 nucleation is effectively shut off on thick templates. Cross-sectional STEM and EDS analysis further verify this "shut-off" mechanism: while active regions show a distinct, chemically sharp WS_2/MoS_2 hetero-stack, the thick-template regions reveal a multilayer MoS_2 surface with no overgrowth (Supplementary Note 5.3). We note that the cross-sectional images also show an atomically continuous TMDC template with no discernible pinholes or open channels within the inspected regions. This structural continuity stands in marked contrast to pinhole- or 'thru-hole'-assisted epitaxy reported in systems with discontinuous spacers [53–55].

Our observations therefore argue against defect-mediated growth pathways, suggesting instead that nucleation is modulated by field penetration through the atomically continuous lattice. These reciprocal-growth experiments show that the remote–vdW hybrid regime is robust to stacking order: in both MoS_2/WS_2 and WS_2/MoS_2, an atomically thin TMDC interlayer sets the in-plane registry wherever growth occurs, while the buried substrate and interlayer thickness jointly control whether nucleation is enabled or suppressed. These findings establish remote–vdW hybrid epitaxy as a general design principle for 2D–2D vertical TMDC heterostructures.

4 Conclusions

In summary, we have demonstrated a substrate-field-modulated remote–vdW hybrid epitaxy regime, where the in-plane registry is dictated by vdW coupling to the 2D template. This approach yields single-orientation heterostructures with no detectable mirror-twin signatures within the examined areas for both reciprocal stacking orders. This dual-control mechanism provides a robust strategy for the deterministic synthesis of high-quality 2D semiconductor heterostructures, addressing key limitations of conventional epitaxial growth. Beyond its role in growth control, the resulting interfacial charge environment may influence the electrical performance of these heterostructures. Potential effects include substrate-induced doping, modified charge-transfer kinetics, and gate-dependent hysteresis, offering a new degree of freedom for substrate-engineered device tuning. Our work establishes a practical framework for the large-area, scalable synthesis of high-quality vertical heterostructures, providing a versatile pathway for developing next-generation electronic and optoelectronic devices with precisely engineered 2D interfaces.

Abbreviations

2D	Two-dimensional
AFM	Atomic force microscopy
CVD	Chemical vapor deposition
DES	Diethyl sulfide
EDS	Energy-dispersive X-ray spectroscopy
FFT	Fast Fourier transform
FIB	Focused ion beam
HAADF-STEM	High-angle annular dark-field scanning transmission electron microscopy
HR-TEM	High-resolution transmission electron microscopy
HS	Heterostructure
ML	Multilayer
MOCVD	Metal–organic chemical vapor deposition
OM	Optical microscopy
PL	Photoluminescence
SAED	Selected-area electron diffraction
STEM	Scanning transmission electron microscopy
TMDC	Transition-metal dichalcogenide
vdW	Van der Waals
WHC	Tungsten hexacarbonyl

Supplementary Information

The online version contains supplementary material available at https://doi.org/10.1186/s40580-026-00542-4.

Additional file1 (DOCX 7068 kb)

Acknowledgements

Not applicable.

Author contributions

W.I.P. conceived the concept and directed the overall research. L.S.H. designed and performed the MOCVD growth experiments, optical characterizations, and led the data analysis. S.J., Y.K., H.Y., D.Y.J., and H.P. assisted with sample preparation (including exfoliation and transfer processes) and supported the experimental data analysis. Z.G. carried out the AFM measurements and analysis under the supervision of J.J. L.S.H. and W.I.P. co-wrote the manuscript. All authors discussed the results and provided critical feedback on the final manuscript.

Funding

This work was supported by the National Research Foundation of Korea (NRF) grant funded by the Ministry of Science and ICT (MSIT) (Nos. RS-2024–00353762, RS-2021-NR060087).

Data availability

The data supporting the findings of this study are available within this article and its Supplementary Information. Source data are provided with this paper.

Declarations

Competing interests

The authors declare no competing interests.

Author details

[1]Division of Materials Science and Engineering, Hanyang University, Seoul 04763, Republic of Korea

Received: 27 December 2025 / Accepted: 6 March 2026

References

1. Y.-Q. Bie, G. Grosso, M. Heuck, M.M. Furchi, Y. Cao, J. Zheng, D. Bunandar, E. Navarro-Moratalla, L. Zhou, D.K. Efetov, A MoTe2-based light-emitting diode

and photodetector for silicon photonic integrated circuits. Nat. Nanotechnol. **12**, 1124 (2017). https://doi.org/10.1038/nnano.2017.209

2. I. Datta, S.H. Chae, G.R. Bhatt, M.A. Tadayon, B. Li, Y. Yu, C. Park, J. Park, L. Cao, D. Basov, Low-loss composite photonic platform based on 2D semiconductor monolayers. Nat. Photon. **14**, 256 (2020). https://doi.org/10.1038/s41566-020-0590-4
3. H. Jiang, Y. Zhang, L. An, Q. Tan, X. Dai, Y. Chen, W. Chen, H. Cai, J. Fu, J. Zúñiga-Pérez, Chiral light detection with centrosymmetric-metamaterial-assisted valleytronics. Nat. Mater. **24**, 1 (2025). https://doi.org/10.1038/s41563-025-02155-4
4. M. Kim, T. Kim, A. Galler, D. Kim, A. Chacon, X. Gong, Y. Yang, R. Fang, K. Watanabe, T. Taniguchi, Quantum interference and occupation control in high harmonic generation from monolayer WS2. Nat. Commun. **16**, 9825 (2025). https://doi.org/10.1038/s41467-025-65725-9
5. K.F. Mak, J. Shan, Photonics and optoelectronics of 2D semiconductor transition metal dichalcogenides. Nat. Photon. **10**, 216 (2016). https://doi.org/10.1038/nphoton.2015.282
6. Q. Shang, K. Dini, H. Jiang, N.W.E. Seet, X. Cai, S. Ru, X. Lu, W.C. Yu, J. Zhao, Q. Xiong, On-chip photonic crystal dressed Rydberg exciton polaritons with enhanced nonlinearity in monolayer WS2. Nat. Commun. **16**, 10352 (2025). https://doi.org/10.1038/s41467-025-65305-x
7. R.T. Victor, S.H. Safeer, J.F. Marroquin, M. Costa, J.F. Felix, V. Carozo, L.C. Sampaio, F. Garcia, Disentangling edge and bulk spin-to-charge interconversion in MoS2 monolayer flakes. Nat. Commun. **16**, 3075 (2025). https://doi.org/10.1038/s41467-025-58119-4
8. J.B. Lee, Y.R. Lim, A.K. Katiyar, W. Song, J. Lim, S. Bae, T.W. Kim, S.K. Lee, J.H. Ahn, Direct synthesis of a self-assembled WSe2/MoS2 heterostructure array and its optoelectrical properties. Adv. Mater. **31**, 1904194 (2019). https://doi.org/10.1002/adma.201904194
9. Y. Kim, B. Kim, S. Jang, M. Kim, H.L. Saptini, S.J. An, W.I. Park, Comparative investigation of interplay between photothermoelectric and photoconductive effects in MoS2 devices. ACS Appl. Electron. Mater. **5**, 6824 (2023). https://doi.org/10.1021/acsaelm.3c01270
10. H. Chen, X. Wen, J. Zhang, T. Wu, Y. Gong, X. Zhang, J. Yuan, C. Yi, J. Lou, P.M. Ajayan, Ultrafast formation of interlayer hot excitons in atomically thin MoS2/WS2 heterostructures. Nat. Commun. **7**, 12512 (2016). https://doi.org/10.1038/ncomms12512
11. P. Rivera, J.R. Schaibley, A.M. Jones, J.S. Ross, S. Wu, G. Aivazian, P. Klement, K. Seyler, G. Clark, N.J. Ghimire, Observation of long-lived interlayer excitons in monolayer MoSe2–WSe2 heterostructures. Nat. Commun. **6**, 6242 (2015). https://doi.org/10.1038/ncomms7242
12. R. Rosati, I. Paradisanos, L. Huang, Z. Gan, A. George, K. Watanabe, T. Taniguchi, L. Lombez, P. Renucci, A. Turchanin, Interface engineering of charge-transfer excitons in 2D lateral heterostructures. Nat. Commun. **14**, 2438 (2023). https://doi.org/10.1038/s41467-023-37889-9
13. E. Barré, O. Karni, E. Liu, A.L. O'Beirne, X. Chen, H.B. Ribeiro, L. Yu, B. Kim, K. Watanabe, T. Taniguchi, Optical absorption of interlayer excitons in transition-metal dichalcogenide heterostructures. Science **376**, 406 (2022). https://doi.org/10.1126/science.abm8511
14. S. Lee, D. Seo, S.H. Park, N. Izquierdo, E.H. Lee, R. Younas, G. Zhou, M. Palei, A.J. Hoffman, M.S. Jang, Achieving near-perfect light absorption in atomically thin transition metal dichalcogenides through band nesting. Nat. Commun. **14**, 3889 (2023). https://doi.org/10.1038/s41467-023-39450-0
15. Y. Xu, S. Liu, D.A. Rhodes, K. Watanabe, T. Taniguchi, J. Hone, V. Elser, K.F. Mak, J. Shan, Correlated insulating states at fractional fillings of moiré superlattices. Nature **587**, 214 (2020). https://doi.org/10.1038/s41586-020-2868-6
16. Q. Tong, H. Yu, Q. Zhu, Y. Wang, X. Xu, W. Yao, Topological mosaics in moiré superlattices of van der waals heterobilayers. Nat. Phys. **13**, 356 (2017). https://doi.org/10.1038/nphys3968
17. Y. Cao, V. Fatemi, S. Fang, K. Watanabe, T. Taniguchi, E. Kaxiras, P. Jarillo-Herrero, Unconventional superconductivity in magic-angle graphene superlattices. Nature **556**, 43 (2018). https://doi.org/10.1038/nature26160
18. Z. Fei, T. Palomaki, S. Wu, W. Zhao, X. Cai, B. Sun, P. Nguyen, J. Finney, X. Xu, D.H. Cobden, Edge conduction in monolayer WTe2. Nat. Phys. **13**, 677 (2017). https://doi.org/10.1038/nphys4091
19. D. Moon, W. Lee, C. Lim, J. Kim, J. Kim, Y. Jung, H.-Y. Choi, W.S. Choi, H. Kim, J.-H. Baek, Hypotaxy of wafer-scale single-crystal transition metal dichalcogenides. Nature **638**, 957 (2025). https://doi.org/10.1038/s41586-024-08492-9
20. T. Chen, D. Ding, J. Shi, G. Wang, L. Kou, X. Zheng, X. Ren, X. Liu, C. Jin, J. Zhong, Lateral and vertical MoSe2–MoS2 heterostructures via epitaxial growth: triggered by high-temperature annealing and precursor concentration. J. Phys. Chem. Lett. **10**, 5027 (2019). https://doi.org/10.1021/acs.jpclett.9b01961
21. H. Heo, J.H. Sung, G. Jin, J.-H. Ahn, K. Kim, M.-J. Lee, S. Cha, H. Choi, M.-H. Jo, Rotation-misfit-free heteroepitaxial stacking and stitching growth of hexagonal transition-metal dichalcogenide monolayers by nucleation kinetics controls. Adv. Mater. **27**, 3803 (2015). https://doi.org/10.1002/adma.201500846
22. X. Zhang, F. Zhang, Y. Wang, D.S. Schulman, T. Zhang, A. Bansal, N. Alem, S. Das, V.H. Crespi, M. Terrones, Defect-controlled nucleation and orientation of WSe2 on hBN: a route to single-crystal epitaxial monolayers. ACS Nano **13**, 3341 (2019). https://doi.org/10.1021/acsnano.8b09230
23. Y. Gong, J. Lin, X. Wang, G. Shi, S. Lei, Z. Lin, X. Zou, G. Ye, R. Vajtai, B.I. Yakobson, Vertical and in-plane heterostructures from WS2/MoS2 monolayers. Nat. Mater. **13**, 1135 (2014). https://doi.org/10.1038/nmat4091
24. R. Wu, Q. Tao, W. Dang, Y. Liu, B. Li, J. Li, B. Zhao, Z. Zhang, H. Ma, G. Sun, Van der Waals epitaxial growth of atomically thin 2D metals on dangling-bond-free WSe2 and WS2. Adv. Funct. Mater. **29**, 1806611 (2019). https://doi.org/10.1002/adfm.201806611
25. S. Jang, L.S. Handriani, H.C. Yun, D.Y. Jeong, Y. Kim, M. Kim, Z. Gao, J.-I. Jang, W.I. Park, Direct and scalable edge-induced alloying of Mo1-xWxS2 via patterned MoS2 templates. Mater. Res. Bull. (2025). https://doi.org/10.1016/j.materresbull.2025.113942
26. J.H. Shin, S. Jang, S.H. Kim, W.J. Chang, J. Kim, S.I. Yang, W.I. Park, Imaging and analysis of multidimensional atomically thin transition metal dichalcogenide layers on diatom frustules. Appl. Surf. Sci. **577**, 151876 (2022). https://doi.org/10.1016/j.apsusc.2021.151876
27. W.J. Chang, S. Jang, M. Kim, Y. Kim, D.Y. Jeong, B. Kim, J.M. Kim, S. Nam, W.I. Park, MoS2 passivated multilayer graphene membranes for Li-ion extraction from seawater. Small **19**, 2207020 (2023). https://doi.org/10.1002/smll.202207020
28. S.S. Kwon, J. Choi, M. Heiranian, Y. Kim, W.J. Chang, P.M. Knapp, M.C. Wang, J.M. Kim, N.R. Aluru, W.I. Park, Electrical double layer of supported atomically thin materials. Nano Lett. **19**, 4588 (2019). https://doi.org/10.1021/acs.nanolett.9b01563
29. G. Hong, Y. Han, T.M. Schutzius, Y. Wang, Y. Pan, M. Hu, J. Jie, C.S. Sharma, U. Muller, D. Poulikakos, On the mechanism of hydrophilicity of graphene. Nano Lett. **16**, 4447 (2016). https://doi.org/10.1021/acs.nanolett.6b01594
30. S. Chae, S. Jang, W.J. Choi, Y.S. Kim, H. Chang, T.I. Lee, J.-O. Lee, Lattice transparency of graphene. Nano Lett. **17**, 1711 (2017). https://doi.org/10.1021/acs.nanolett.6b04989
31. D. Lee, J.J. Lee, Y.S. Kim, Y.H. Kim, J.C. Kim, W. Huh, J. Lee, S. Park, H.Y. Jeong, Y.D. Kim, Remote modulation doping in Van der Waals heterostructure transistors. Nat. Electron. **4**, 664 (2021). https://doi.org/10.1038/s41928-021-00641-6
32. H. Ryu, H. Park, J.-H. Kim, F. Ren, J. Kim, G.-H. Lee, S.J. Pearton, Two-dimensional material templates for van der Waals epitaxy, remote epitaxy, and intercalation growth. Appl. Phys. Rev. (2022). https://doi.org/10.1063/5.0090373
33. Y.J. Hong, W.H. Lee, Y. Wu, R.S. Ruoff, T. Fukui, Van der waals epitaxy of InAs nanowires vertically aligned on single-layer graphene. Nano Lett. **12**, 1431 (2012). https://doi.org/10.1021/nl204109t
34. Y.J. Hong, J.W. Yang, W.H. Lee, R.S. Ruoff, K.S. Kim, T. Fukui, Van der waals epitaxial double heterostructure: InAs/single-layer graphene/InAs. Adv. Mater. **25**, 6847 (2013). https://doi.org/10.1002/adma.201302312
35. Y. Kim, S.S. Cruz, K. Lee, B.O. Alawode, C. Choi, Y. Song, J.M. Johnson, C. Heidelberger, W. Kong, S. Choi, Remote epitaxy through graphene enables two-dimensional material-based layer transfer. Nature **544**, 340 (2017). https://doi.org/10.1038/nature22053
36. W. Kong, H. Li, K. Qiao, Y. Kim, K. Lee, Y. Nie, D. Lee, T. Osadchy, R.J. Molnar, D.K. Gaskill, Polarity governs atomic interaction through two-dimensional materials. Nat. Mater. **17**, 999 (2018). https://doi.org/10.1038/s41563-018-0176-4
37. C. Chang, X. Zhang, W. Li, Q. Guo, Z. Feng, C. Huang, Y. Ren, Y. Cai, X. Zhou, J. Wang, Remote epitaxy of single-crystal rhombohedral WS2 bilayers. Nat. Commun. **15**, 4130 (2024). https://doi.org/10.1038/s41467-024-48522-8
38. J. Jeong, Q. Wang, J. Cha, D.K. Jin, D.H. Shin, S. Kwon, B.K. Kang, J.H. Jang, W.S. Yang, Y.S. Choi, Remote heteroepitaxy of GaN microrod heterostructures for deformable light-emitting diodes and wafer recycle. Sci. Adv. **6**, eaaz5180 (2020). https://doi.org/10.1126/sciadv.aaz5180
39. J. Jeong, K.-A. Min, D.H. Shin, W.S. Yang, J. Yoo, S.W. Lee, S. Hong, Y.J. Hong, Remote homoepitaxy of ZnO microrods across graphene layers. Nanoscale **10**, 22970 (2018). https://doi.org/10.1039/C8NR08084D
40. Y.-P. Chang, W.-B. Li, Y.-C. Yang, H.-L. Lu, M.-F. Lin, P.-W. Chiu, K.-I. Lin, Oxidation and degradation of WS2 monolayers grown by NaCl-assisted chemical vapor

deposition: mechanism and prevention. Nanoscale **13**, 16629 (2021). https://doi.org/10.1039/D1NR04809K
41. H. Zeng, G.-B. Liu, J. Dai, Y. Yan, B. Zhu, R. He, L. Xie, S. Xu, X. Chen, W. Yao, Optical signature of symmetry variations and spin-valley coupling in atomically thin tungsten dichalcogenides. Sci. Rep. **3**, 1608 (2013). https://doi.org/10.1038/srep01608
42. J. Park, M.S. Kim, E. Cha, J. Kim, W. Choi, Synthesis of uniform single layer WS2 for tunable photoluminescence. Sci. Rep. **7**, 16121 (2017). https://doi.org/10.1038/s41598-017-16251-2
43. W. Zhao, Z. Ghorannevis, L. Chu, M. Toh, C. Kloc, P.-H. Tan, G. Eda, Evolution of electronic structure in atomically thin sheets of WS2 and WSe2. ACS Nano **7**, 791 (2013). https://doi.org/10.1021/nn305275h
44. M. Amani, D.-H. Lien, D. Kiriya, J. Xiao, A. Azcatl, J. Noh, S.R. Madhvapathy, R. Addou, S. Kc, M. Dubey, Near-unity photoluminescence quantum yield in MoS2. Science **350**, 1065 (2015). https://doi.org/10.1126/science.aad2114
45. A. Laturia, M.L. Van de Put, W.G. Vandenberghe, Dielectric properties of hexagonal boron nitride and transition metal dichalcogenides: from monolayer to bulk. npj 2D Mater. Appl. **2**, 6 (2018). https://doi.org/10.1038/s41699-018-0050-x
46. H. Fang, M. Tosun, G. Seol, T.C. Chang, K. Takei, J. Guo, A. Javey, Degenerate n-doping of few-layer transition metal dichalcogenides by potassium. Nano Lett. **13**, 1991 (2013). https://doi.org/10.1021/nl400044m
47. M.M. Ugeda, A.J. Bradley, S.-F. Shi, F.H. Da Jornada, Y. Zhang, D.Y. Qiu, W. Ruan, S.-K. Mo, Z. Hussain, Z.-X. Shen, Giant bandgap renormalization and excitonic effects in a monolayer transition metal dichalcogenide semiconductor. Nat. Mater. **13**, 1091 (2014). https://doi.org/10.1038/nmat4061
48. N. Nayir, S. Bartolucci, T. Wang, C. Chen, J. Maurer, J.M. Redwing, A.C. van Duin, Modulation effect of substrate interactions on nucleation and growth of MoS2 on silica. J. Phys. Chem. C **127**, 9039 (2023). https://doi.org/10.1021/acs.jpcc.3c01010
49. M. Lawson, E. Graugnard, L. Li, First-principles studies of MoF6 absorption on hydroxylated and non-hydroxylated metal oxide surfaces and implications for atomic layer deposition of MoS2. Appl. Surf. Sci. **541**, 148461 (2021). https://doi.org/10.1016/j.apsusc.2020.148461
50. M. Shirazi, W. Kessels, A. Bol, Initial stage of atomic layer deposition of 2D-mos 2 on a sio 2 surface: A DFT study. Phys. Chem. Chem. Phys. **20**, 16861 (2018). https://doi.org/10.1039/C8CP00210J
51. J. Sitek, J. Plocharski, I. Pasternak, A.P. Gertych, C. McAleese, B.R. Conran, M. Zdrojek, W. Strupinski, Substrate-induced variances in morphological and structural properties of MoS2 grown by chemical vapor deposition on epitaxial graphene and SiO2. ACS Appl. Mater. Interfaces **12**, 45101 (2020). https://doi.org/10.1021/acsami.0c06173
52. S. Paul, R. Torsi, J.A. Robinson, K. Momeni, Effect of the substrate on MoS2 monolayer morphology: An integrated computational and experimental study. ACS Appl. Mater. Interfaces **14**, 18835 (2022). https://doi.org/10.1021/acsami.2c03471
53. D. Jang, C. Ahn, Y. Lee, S. Lee, H. Lee, D. Kim, Y. Kim, J.Y. Park, Y.K. Kwon, J. Choi, Thru-hole epitaxy: A highway for controllable and transferable epitaxial growth. Adv. Mater. Interfaces **10**, 2201406 (2023). https://doi.org/10.1002/admi.202201406
54. C.S. Chang, K.S. Kim, B.-I. Park, J. Choi, H. Kim, J. Jeong, M. Barone, N. Parker, S. Lee, X. Zhang, Remote epitaxial interaction through graphene. Sci. Adv. **9**, eadj5379 (2023). https://doi.org/10.1126/sciadv.adj5379
55. H. Lee, M. Kim, D. Jang, S. Jang, W.I. Park, C. Kim, Transferable thru-hole epitaxy of gan and ZnO, respectively, over graphene and MoS2 as a 2D space layer. Cryst. Growth Des. **22**, 6995 (2022). https://doi.org/10.1021/acs.cgd.2c00660

Publisher's Note